# Pt-Sn-Co Nanocubes as Highly Active Catalysts for Ethanol Electro-Oxidation

Rubén Rizo[1], Arno Bergmann[1], Janis Timoshenko[1], Fabian Scholten[1], Clara Rettenmaier[1], Hyo Sang Jeon[1], Yen-Ting Chen[2], Aram Yoon[1], Alexander Bagger[3], Jan Rossmeisl[3], Beatriz Roldan Cuenya[1*]

[1] *Department of Interface Science, Fritz-Haber Institute of the Max-Planck Society, 14195 Berlin, Germany*

[2] *Department of Physics, Ruhr-University Bochum, 44780 Bochum, Germany*

[3]*Department of Chemistry, University of Copenhagen, Universitetsparken 5, Copenhagen, 2100, Denmark*

Corresponding author: roldan@fhi-berlin.mpg.de



## Abstract

Direct ethanol fuel cells are among the most promising clean electrochemical power sources. Nevertheless, the high cost and low efficiency of the Pt-based catalysts hinder their commercialization. Here, Pt-Sn-Co nanocubes with a Pt- and Sn-rich shell show improved performance towards the electrochemical ethanol oxidation reaction. Mechanistic and structural insights were obtained by synergistically combining different *in situ* and *operando* spectro-electrochemical techniques, including electrochemical mass spectrometry, X-ray photoelectron spectroscopy and X-ray absorption spectroscopy. In particular, electrochemical conditioning and EOR were found to induce Sn leaching from the core and shell, leading to electrochemically-accessible Pt sites adjacent to partially-oxidized Sn sites on a $Pt_3Co$-like core. The increased activity of the Pt-Sn-Co nanocubes was assigned to the formation of a higher amount of $C_1$ ($CO_2$) and $C_2$ (acetic acid/acetaldehyde) products during EOR as well as

to their high ability to remove adsorbed CO from the Pt surface when compared to similarly-sized cubic Pt-Sn or Pt NPs. Beneficial strain and ligand effects are combined here through a catalyst design resulting in adjacent Pt and Sn sites at the overlayer on top of a $Pt_3Co$ alloy core.

**Keywords:** Pt-Sn-Co nanocubes, core-shells, DEMS, ethanol oxidation reaction, XAS, XRD, TEM, XPS

## 1. Introduction

During the last decades, significant effort has been dedicated to the development of technologies for electrochemical energy conversion in order to address the global energy challenge[1–3]. Direct ethanol fuel cells (DEFC) have been postulated as an attractive alternative to fossil fuels in certain applications[4,5]. The utilization of ethanol entails multiple advantages. Since it is a liquid fuel, storage and transportation problems associated with the use of gases as fuels are minimized. Moreover, it is a renewable and eco-friendly fuel that can be obtained directly from the fermentation of biomass. In contrast to methanol, it is less toxic and its complete oxidation leads to higher energy densities[6]. Nevertheless, some disadvantages in the use of such sustainable systems hinder their commercialization. The main problem relies on the electrocatalyst material itself, since Pt has been postulated as the most electroactive pure metal for the ethanol oxidation reaction (EOR). However, Pt is an expensive noble metal prone to deactivation during the EOR by the adsorption of monocarbon species (CO and $CH_x$) which block active sites[7,8]. In order to circumvent these problems, Pt nanoparticles (NPs) with high surface area have been used in addition to more complex material systems that combine Pt with other less expensive metals such as Ru[9,10], Co[11] or Sn[12,13]. The presence of these secondary metals appears to facilitate the oxidation of the poisoning intermediates at lower

overpotentials than in the case of pure Pt[14], lowering the rate of catalyst deactivation. In particular, Pt-based catalysts composed by a Pt-overlayer surface structure (few monolayers of Pt on the surface) are very stable and active for many electrochemical reactions, due to their altered electronic properties and the shortening of the surface Pt-Pt bond distances induced by the underlying transition metals in subsurface layers[15]. Furthermore, trimetallic Pt-based electrocatalysts have been designed as a new strategy to improve, not only the tolerance of the catalysts to poisoning intermediates but also the C-C bond cleavage capability[12,16–18]. For example, a combination of Pt with an oxhophilic metal and Rh has been proposed for this purpose. However, despite the good capability of Rh to break the C-C bond, it is also prone to deactivation by CO[19].

In addition, the EOR has been found to be a structure-sensitive reaction, where the Pt(100) basal plane is the one that results in the highest current[20,21]. Thus, the synthesis of electrocatalysts consisting of shape-controlled Pt-based NPs with preferential (100) orientation is desired in order to bring the electrocatalytic performance to a level that would make DEFC attractive for industrial applications, including those in the area of transportation. Only a few studies have been dedicated this far to the synthesis of Pt-based cubic EOR electrocatalyst[4,16,22–26], and only one work has reported the study of trimetallic Pt-based cubic nanocrystals.[26]

The present work describes the synthesis of (100)-exposing Pt-Sn-Co core-shell electrocatalysts with outstanding activity for EOR and provides insights into the reaction mechanism based on *ex situ* electron microscopy, electrochemical characterization, *in situ*/*operando* spectro-electrochemical and diffraction methods.

## 2. Results and discussion

### 2.1 Nanoparticle morphology

Pt-Sn-Co nanoparticles were synthesized by the solvothermal route in Ar atmosphere using oleylamine and oleic acid as structure-directing agents and tungsten carbonyl as reducing agent. Pt-Sn and Pt nanocubes were prepared using the same synthesis route for comparison. ADF-STEM was applied to confirm the cubic morphology of the Pt-Sn-Co NPs. Figure 1(a) shows predominantly cubic nanoparticles (nanocubes, NCs) with well-defined {100} facets, exhibiting a homogeneous size distribution with an edge length of 9.2 ± 0.4 nm (Figure S1a, Table 1). The Pt-Sn-Co nanocubes are homogeneously distributed on the carbon support, Figure 1(b). The distribution of Pt, Sn and Co atoms within the as-prepared nanocubes was confirmed by ADF-STEM combined with EDX line scans and maps, Figure 1(c-d) and (e-h), respectively. The EDX maps suggest that the as-prepared nanocubes have a core-shell structure, with Sn mostly distributed in the shell and Co in the core. The average composition of the as-prepared nanocube shell is about 48 at.% Pt, 51 at.% Sn and 1 at.% Co, while the composition of the core is approx. 78 at.% Pt, 15 at.% Sn and 7 at.% Co.

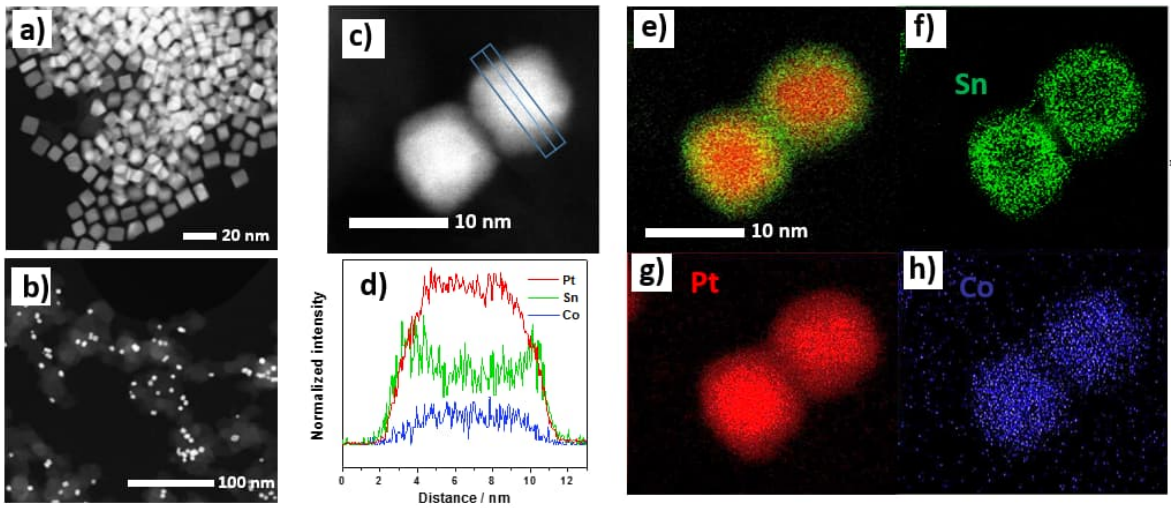


**Figure 1.** STEM images of the (a) as-prepared unsupported cubic Pt-Sn-Co NPs. (b) Low-magnification ADF-STEM images of the NPs supported on Vulcan XC-72R. (d) EDX line-profiles recorded across the regions indicated by the arrow in (c). (e-h) EDX composition maps, showing Sn (green, f), Pt (red, g) and Co (blue, h) distributions.

High resolution TEM (HRTEM) images combined with fast Fourier transform (FTT) analysis (Figure S1b) display clear (200) and (220) lattice fringes with the interplanar spacings of 0.196 and 0.232 nm, respectively, implying that the Pt-Sn-Co nanocubes are in fact enclosed by {100} planes. However, the rounded corners of the nanocubes indicate that the cubes expose multiple other facets, as indicated in the model displayed in Figure S1c.

The XRD patterns from Figure 2 of the as-prepared Pt-Sn-Co nanocubes, as well as those of pure Pt, and Pt-Sn NCs, with similar particle size (Table 1) chosen for comparison, exhibit peaks typical for the face-centered cubic (fcc) Pt (alloy) phases and for graphitic carbon[27].

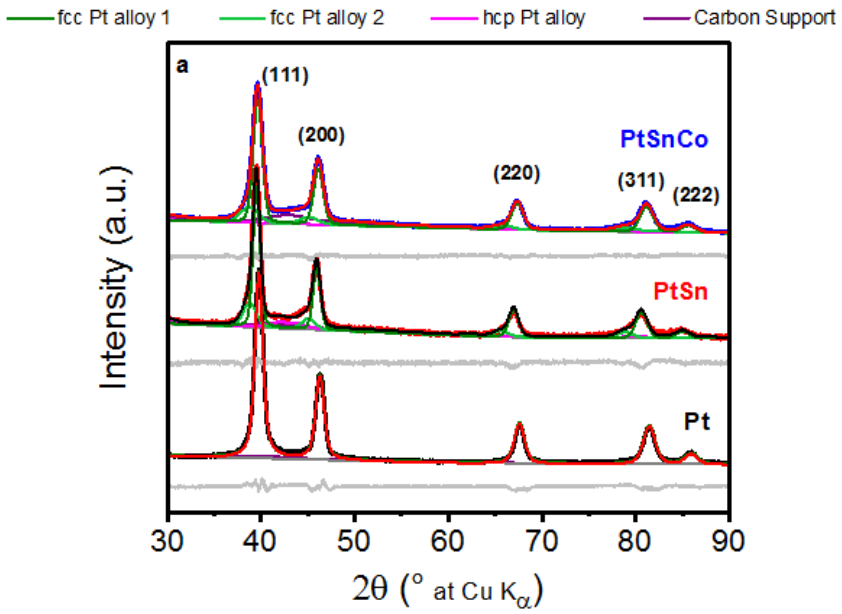


**Figure 2.** XRD patterns of the as-prepared Pt, Pt−Sn and Pt-Sn-Co nanocubes supported on carbon (Vulcan XC-72R) were recorded in the as-prepared state and after electrochemical potential cycling. The fitted profiles were extracted by using Rietveld refinement. The experimental data of Pt, Pt-Sn, and Pt-Sn-Co are shown in black, red and blue, respectively. The fitted profiles are shown in red. The individual contributions from the fcc phase 1 (dark green), fcc phase 2 (light green), hcp phase (magenta), and from the carbon support (violet) are also shown as well as the corresponding background (dark grey) and difference curves (light grey).

No crystalline Co- or Sn-containing oxide phases were identified using XRD but a secondary fcc PtM alloy phase was identified in the case of the Pt-Sn and Pt-Sn-Co nanocubes. This PtM alloy phase exhibits an expanded lattice and a lower structural coherence length as the diffraction peaks appear at lower diffraction angles and are significantly broader than the main fcc Pt phase. Rietveld refinement was performed to quantify the different phases and extract their structural properties (Table S1). Table 1 depicts the lattice parameter of the main fcc phase and the crystallite size for the three samples.

| | TEM Particle size (nm) | XRD Crystallite size (nm) | Lattice parameter (Å) |
|---|---|---|---|
| Pt | 8.2 ± 1.6 | 7.48 ± 0.06 | 3.9161 ± 0.0002 |
| Pt-Sn | 10.6 ± 0.4 | 11.0 ± 0.3 | 3.9565 ± 0.0005 |
| Pt-Sn-Co | 9.2 ± 0.4 | 7.8 ± 0.1 | 3.9259 ± 0.0009 |

**Table 1**. Morphological and structural parameters of cubic NPs synthesized by solvothermal methods obtained from TEM and XRD. The TEM particle size values for Pt and Pt-Sn samples have been extracted from our previous work[4]. The XRD crystallite size and the lattice parameter were determined using Rietveld refinement for the main fcc Pt alloy phase reflecting the nanocube core.

The lattice parameter of the main fcc phase was found to be the lowest for the Pt nanocubes with 3.9161 ± 0.0002 Å and the largest for Pt-Sn with 3.9565 ± 0.0005 Å, which is attributed to the incorporation of the larger Sn atoms into the Pt host lattice. The lattice parameter of fcc PtM alloys is known to increase with increasing atomic radius of the secondary metal species[28]. For Pt-Sn-Co, an intermediate lattice parameter of 3.9259 ± 0.0009 Å was determined, which is in agreement with the lattice spacing identified in the HRTEM images and shows the incorporation of the smaller Co atoms into the expanded PtSn host lattice. The lattice parameters of the secondary fcc Pt alloy phase were determined to be 4.029 ± 0.002 Å and 4.002 ± 0.002 Å for the Pt-Sn and Pt-Sn-Co nanocubes, respectively, and agree well with a fcc $Pt_3Sn$ phase. The structural coherence length of the main fcc phase was determined to be 7.48 ± 0.06 nm for Pt, 11.0 ± 0.3 nm for Pt-Sn, and 7.82 ± 0.13 nm for Pt-Sn-Co nanocubes, whereas the secondary fcc phase exhibits a structural coherence length of 4.5 ± 0.3 nm and 2.92 ± 0.11 nm for the Pt-Sn and Pt-Sn-Co NCs, respectively. The secondary fcc PtM alloy phase contributes with ~15 and 30 wt.% for Pt-Sn and Pt-Sn-Co, respectively. In the case of the Pt-Sn NCs, Rietveld refinement also suggests the presence of a hexagonal PtSn alloy.

Combining the STEM-EDX and XRD findings, the main fcc PtM alloy phase most likely reflects the core of the nanocubes, and the shell (at least partially) consists of the secondary fcc PtM alloy phase and/or the hexagonal metal phases. The expanded lattice parameter of the secondary phases agrees well with the Sn accumulation in the nanocube shell compared to the core, although being Pt-rich in the metallic domains. The deviation in the shell composition can be explained on the one hand by the cumulative nature of shell and core signals in the STEM-EDX maps inhibiting a straightforward quantitative determination of the composition. On the other hand, X-ray diffraction is only sensitive to crystalline phases, and very small and/or amorphous oxide domains are not detectable. Furthermore, the structural coherence lengths of the metal phases in the nanocubes were determined based on the coherence length of spherical NPs of a similar volume as the cubic domains. Applying this approximation, the crystalline cores of the nanocubes exhibit an edge length of 4-6 nm, in good agreement with the core size determined by STEM-EDX for the Pt-Sn-Co nanocubes.

### 2.2 Electrochemical characterization and EOR catalytic activity

The catalytic activity and selectivity of the Pt-Sn-Co nanocubes during ethanol oxidation reaction were investigated and compared to Pt-Sn and Pt NCs with similar size, whose XRD patterns were shown in section 3.1. Prior to the catalytic testing, the Pt-Sn-Co nanocubes were electrochemically activated using cyclic voltammetry in 0.5 M $H_2SO_4$ as shown in Figure 3a.

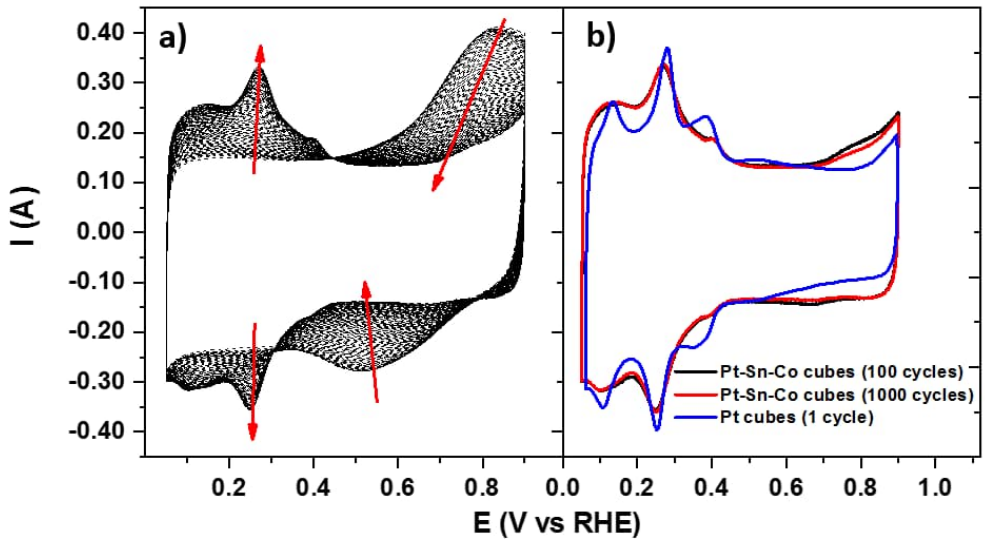


**Figure 3.** (a) Evolution of the cyclic voltammetry during 100 cycles and (b) comparison between the cyclic voltammetry after 100 cycles and after 1000 cycles for the as-prepared Pt-Sn-Co/C catalyst and the cyclic voltammetry of Pt cubes after 1 cycle in Ar-purged 0.5 M $H_2SO_4$ at 50 mV/s.

While the reversible Pt hydrogen adsorption/desorption peaks are not visible in the first cycle, two peaks evolve in the region between 0.05 V and 0.45 V characteristic of a clean Pt surface[29] in the course of 1000 cyclic voltammograms (CVs). The peak at 0.27 V and a feature centered at 0.37 V are associated with hydrogen adsorption/desorption on (100) steps and long (100) domains, respectively,[30] and are characteristic of a clean Pt(100) surface. Simultaneously, redox features above 0.50 V decrease tremendously, suggesting significant changes in the surface structure and composition of the Pt-Sn-Co nanocubes. A stable state of the Pt-Sn-Co is reached after 100 cycles, suggesting a high electrochemical microstructural stability of the Pt-Sn-Co nanocubes (Figure 3b).

The evolution of the CVs is in good agreement with the formation of electrochemically accessible Pt sites due to Sn leaching from the Pt-Sn-Co shell. Sn covers the H adsorption sites on the Pt in the as-prepared state and causes the pronounced redox feature above 0.5 V. During

the continuous potential cycling, Sn leaches into the acidic electrolyte generating accessible Pt adsorption sites. This is in agreement with a previous work on Pt-Sn catalysts describing partial leaching of Sn from the surface of the electrocatalyst after cycling in a 0.5 M $H_2SO_4$ electrolyte leading to a Pt overlayer[4].

Interestingly, the CV of the Pt nanocubes shows not only the typical peaks of the (100) facets but also a peak at 0.16 V, attributed to (110)-type sites [31]. This peak is almost negligible in the CV profile of the Pt-Sn-Co nanocubes, which shows the low density of defects on the Pt surface after electrochemical activation. The rounded corners of the Pt-Sn-Co nanocubes thus, most likely remain covered with Sn.

Hence, an activation pre-treatment of 100 cycles in 0.5 M $H_2SO_4$ was applied prior to any electrochemical measurement of the Pt-Sn-Co nanocubes as well as those of the Pt-Sn and Pt nanocube reference materials.

The catalytic activity towards EOR (0.5 M $H_2SO_4$ + 1 M ethanol) of the three catalysts as tested using cyclic voltammetry is shown in Figure 4a. The currents were normalized by the CO-ECSA calculated from the CO stripping charge instead of using the hydrogen adsorption/desorption charge due to the higher accuracy of the latter method for Pt-based catalysts. This is especially relevant in the case where oxygenated species might be adsorbed on Pt or possible redox processes from the secondary metals might take place in the hydrogen adsorption/desorption region[32–34]. The catalytic activity and stability normalized to the Pt mass is shown in the supporting information (Figure S2).

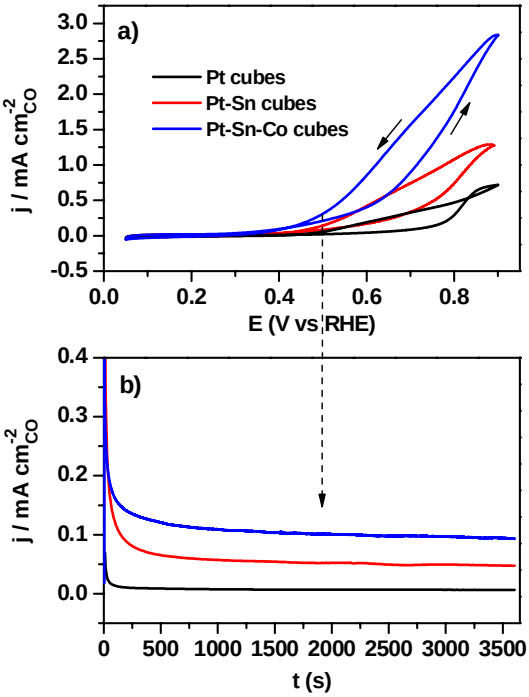


**Figure 4.** (a) Comparison of EOR curves at a scan rate of 20 $mVs^{-1}$ and (b) current transients at 0.50 V (from an initial potential of +0.05 V) of the Pt/C (black), Pt–Sn/C (red), and Pt-Sn-Co/C NP (blue) samples after 100 cycles activation in Ar-purged 0.5 M $H_2SO_4$ + 1 M EtOH solution. Currents are normalized by the ECSA calculated from the electrooxidation of an adsorbed CO monolayer.

The cyclic voltammograms of the Pt-based nanocubes show the typical EOR profiles in which anodic scans show lower current densities than the cathodic scans. The Pt-Sn-Co nanocubes show the highest electrocatalytic activity among the three samples, following: Pt-Sn-Co > Pt-Sn > Pt. Furthermore, the Pt-Sn-Co nanocubes exhibit a surprisingly low onset potential for EOR (0.30 V) in comparison to the Pt-Sn (0.40 V) and Pt nanocubes (0.58 V). It is worth to mention that a similarly low onset potential for EOR in acidic media has been recently reported for PtAuSn catalyst supported on tungsten carbide[35]. However, the reported currents were 50 times lower than those achieved here for the PtSnCo NCs.

This superior performance of the Pt-Sn-Co electrocatalyst and its stability against poisoning intermediates during extended reaction times was further confirmed by chronoamperometry. Therefore, the electrode potential was stepped from the catalytically-inactive state (0.05 mV) to an EOR potential typical for fuel cell conditions (0.5 V), Figure 4b and Figure S2b. The profiles for the three electrocatalysts show a typical current decay in the first 300 s followed by a stationary current at longer reaction times. The initial current decay can be explained by the strong adsorption of poisoning intermediates, such as $(CO)_{ad}$ or $(CH_x)_{ad}$ formed during the oxidation of ethanol. The Pt-Sn-Co nanocubes displayed the best specific activity with stationary currents two times higher than that of Pt-Sn NCs and twelve times higher than Pt NCs.

### 2.3 Mechanistic investigations of EOR

To understand the improved performance of the Pt-Co-Sn catalyst as compared to Pt-Sn and Pt, DEMS and CO stripping experiments were carried out.

DEMS was employed to follow the different volatile products and intermediates formed during the EOR and to get mechanistic insight into the electrochemical reactions. Figure 5 shows the CVs and the MSCVs acquired on Pt, Pt-Sn and Pt-Sn-Co nanocubes tracking the current (CO-ECSA normalized), as well as the formation of $CO_2$ (m/z = 22, fragment $[CO_2]^{++}$), of methane and acetaldehyde (m/z = 15, fragment $[CH_3]^+$ from both compounds) and acetic acid (indirectly via ethylacetate ester formed by the reaction of acetic acid with ethanol in solution[36], m/z =61, fragment $[CH_3CH_2CH_2\text{-}OH_2]^{\cdot+}$).

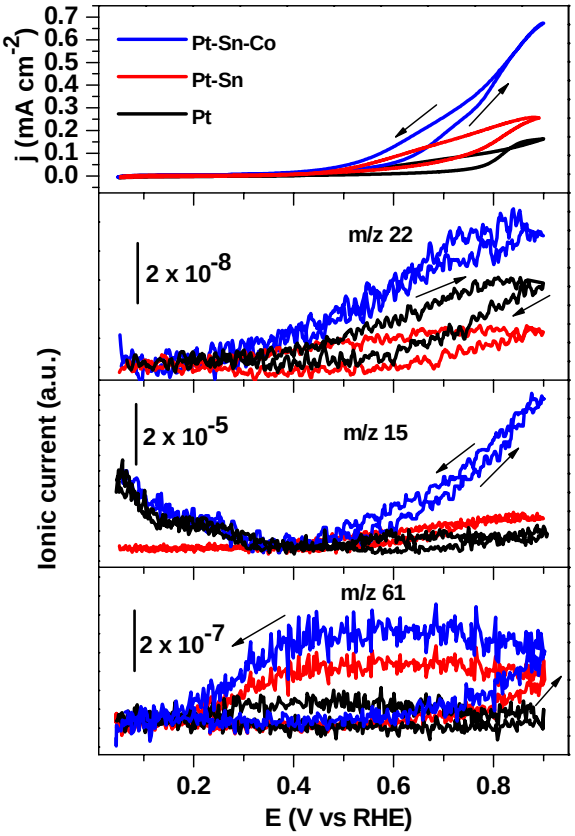


**Figure 5.** CVs (bottom panel) and MSCVs for m/z = 22, m/z = 15 and m/z = 61 over Pt, Pt–Sn and Pt-Sn-Co nanocubes in 0.1 M EtOH + 0.5 M $H_2SO_4$ recorded at room temperature and 5mV$s^{-1}$ The ionic currents are normalized by the integrated corresponding signal for the CO2 (m/z = 44) generated during CO stripping

The MSCV profiles show that the Pt-Sn-Co nanocubes exhibit a higher $CO_2$ production (m/z =22) and almost the same amount of methane (m/z = 15, E < 0.35 V) as the Pt NCs, whereas the Pt-Sn NCs show the lowest amounts of these products. A detailed inspection of the of $CO_2$ signal reveals that the onset potentials are 0.30, 0.40 and 0.50 V for Pt-Sn-Co, Pt-Sn and Pt NCs, respectively, and thus, the low EOR onset potential of the PtSnCo NCS can be assigned to the oxidation of ethanol to $CO_2$. Similarly, the onset potential for acetaldehyde formation increases for Pt-Sn-Co, Pt-Sn and Pt, with values of 0.35, 0.40 and 0.56 V,

respectively. The maximum acetaldehyde formation rate shows the same trend. Thus, the formation of $C_1$ and $C_2$ products formation is promoted by the addition of Co to the bimetallic Pt-Sn electrocatalyst.

CO is a poisoning intermediate formed during EOR and thus, the ability of the synthesized catalysts to oxidize CO was investigated using cyclic voltammetry and differential electrochemical mass spectrometry (DEMS). Figure 6 shows the CVs and the MSCVs of Pt and Pt-Sn-Co nanocubes for the oxidation of a CO-poisoned and a CO-free surface after CO stripping. The analogous data for the Pt-Sn nanocubes are shown in the supporting information (Figure S3).

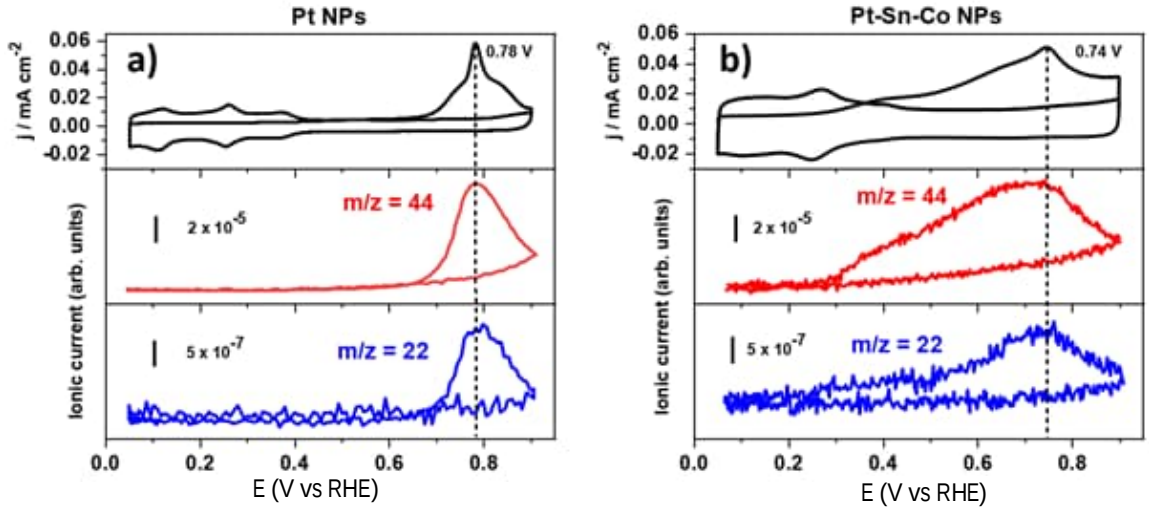


**Figure 6.** Simultaneously recorded CV (upper panel) and MSCVs for $m/z = 22$ (middle panel), $m/z = 44$ (lower panel) during CO stripping experiments on (a) Pt and (b) Pt-Sn-Co nanocubes, in 0.5 M $H_2SO_4$ at 5 mV/s. The currents are normalized by the electrochemically-active surface area calculated from the CO stripping charge (CO-ECSA). The mass to charge (m/z) ratio m/z = 44 and m/z = 22 are attributed to the ionic currents of carbon dioxide $[CO_2]^+$ and doubly ionized carbon dioxide $[CO_2]^{++}$ species, respectively.

The CO stripping experiments for the Pt-Sn catalyst (see supporting information, Figure S3) show an earlier onset potential (0.30 V), as compared to pure Pt nanocubes (0.60 V), while the position of the main peak is the same as for Pt (0.78 V). An earlier onset potential (0.25 V)

was obtained for Pt-Sn-Co in the CO stripping experiments, with the main peak at slightly lower potential (0.74 V), as compared to Pt and Pt-Sn NCs. Both, the onset potential and the position of the main CO oxidation peak are an important parameter for EOR electrocatalysts, as a lower onset and main peak potentials lead to a higher CO oxidation rate at EOR-relevant potentials and thus, reflects a higher ability of the catalyst surface to oxidize CO under EOR conditions. Thus, we can conclude that this ability increases in the order Pt < Pt-Sn < Pt-Sn-Co. Interestingly, the oxidation of CO seems to take place in a broader potential range in Pt-Sn and Pt-Sn-Co NCs as compared to the pure Pt NC catalyst, which suggests that the CO diffusion over the Pt surface might be more hindered due to the presence of (cationic) Sn species and/or Sn oxide domains.

Combining the DEMS results for EOR and CO striping experiments allows us to gain understanding on the reaction mechanism over the Pt-Sn-Co surface as compared to Pt-Sn and pure Pt. The DEMS experiments in Figure 5 show oxidation towards partly oxidized $C_2$ products (acetaldehyde), which we believe is an effect of the surface being partly poisoned by carbon species (CO* or alike), similarly to our previous investigations of propene oxidation[37]. It is plausible that these carbon species cover the surface leaving only a few free sites. This limits the C-C bond breaking, making more favorable the formation of $C_2$ products. Mechanistically, this suggests that pristine Pt can break the C-C bond, and that pristine Pt is limited by too strongly adsorbed carbon species. Hence, EOR at Pt can be improved in two ways: (i) providing oxygen species to the surface at a lower potential and (ii) a slight deactivation of Pt making Pt less prone to being poisoned by carbon species.

For Pt-Sn the CO stripping experiments show an earlier onset potential as compared to Pt, while the main peak is similar to Pt, see Figure S3 The early onset is observed due to the presence of Sn, which provides oxyphilic sites (i), and hence is able to make oxygen available

to lower the oxidation potential[38]. The main peak, however, relates to the situation where most sites on the surface are able to catalyze the oxidation, which is the same on Pt and Pt-Sn.

For Pt-Sn-Co the CO stripping experiments in Figure 6(b) show an earlier onset potential for CO oxidation and the main peak at a slightly lower potential as compared to Pt. The main oxidation peak at lower potential shows the core-shell nature of the Pt-Sn-Co system, where the surface Pt sites display a weaker CO bonding than pure Pt. Based on the strain effect theory, the $Pt_3Co$-like core exhibits a contracted lattice which may alter the properties of the Pt surface via the compression of the Pt-rich overlayer[39,40]. On the other hand, according to the ligand effect theory, Pt and Co in the $Pt_3Co$ core interact directly with each other, which may result in a decrease of the electron density of the Pt-rich overlayer[41,42]. Both, strain and ligand effects on Pt surfaces, induced by the presence of Co, cause a shift in the d-band center of the Pt overlayer away from the Fermi level that has been demonstrated weakens the surface-adsorbate bond and enhances the CO oxidation rate on the Pt overlayer[39–42]. Thus, the combination of the slightly deactivated Pt (ii) with the increased access of oxygen (i) makes the Pt-Sn-Co NCs outperform Pt and Pt-Sn NCs for EOR.

The fact that the addition of Co results in a more favorable complete oxidation of ethanol can be realized by comparing the $CO_2$ conversion efficiencies during the forward EOR, leading to 5.0%, 3.5% and 2.4% for Pt, Pt-Sn-Co and Pt-Sn NCs, respectively. To the best of our knowledge, the highest current efficiencies reported to date, 8.6% for Pt/TiOC and and 6.5% for PtRh/Carbon-Vulcan[43,44], were acquired with an ethanol concentration of 0.1 M. However, using similar conditions to the ones employed here, no efficiencies higher than 2.6% have been described for carbon-supported Pt-based catalysts containing non-noble metals[45]. Nevertheless, 6.5% efficiency in 0.5 M ethanol was demonstrated for a PtAuSn catalyst deposited on tungsten carbide, although it was not clear here if the good performance could be

alsolargely attributed to the influence of the catalyst support[35]. Thus, our Pt-Sn-Co NCs with a conversion efficiency to $CO_2$ of 3.5% are a highly promising electrocatalysts for EOR which might be further improved by using a more optimum catalyst support.

### 2.4 Dynamic evolution of the nanocube structure and chemical state after EOR

The electrochemical and electrocatalytic investigation unraveled on the one hand an excellent catalytic activity of the Pt-Sn-Co nanocubes but on the other hand, they also revealed major changes in the structure, composition and potentially of the morphology of the NCs. Thus, the physicochemical characterization was conducted after different stages of electrochemical characterization to gain better insight into the electrochemically-formed catalysts as well as the catalytically-active state by *in situ* X-ray absorption spectroscopy.

The changes in the crystalline structure of the Pt-Sn-Co nanocubes after 1000 potential cycles in 1M EtOH + 0.5M $H_2SO_4$ were investigated using synchrotron-based high energy XRD and excerpts of the diffraction patterns are shown in Figure 7a. The structural coherence length of the main fcc Pt alloy phase decreased to 5.7 ± 0.1 nm as well as the lattice parameter to 3.871 ± 0.002 Å after electrochemical potential cycling. This finding agrees well with the formation of a $Pt_3Co$-like alloy core. Additionally, the fraction of the secondary fcc PtSn alloy significantly decreased and contributed only ~5 wt.% of the metal phases. Thus, electrochemical cycling leads to a smaller and presumably Sn-poor $Pt_3Co$ core and a significantly reduced contribution of the PtSn component in the shell. This can be explained by Sn leaching during potential-induced redox cycles not only from the surface of the nanocubes but also from the core, decreasing the structural coherence length of the nanocube core. This

phenomenon is well known from the electrochemical dealloying of PtM alloy catalysts for the oxygen reduction reaction and agrees well with the evolution of the cyclic voltammograms.

Figure 7b shows the ADF-STEM image of the Pt-Sn-Co catalyst after reaction, which reveals that the nanocubes maintained their morphology as well as good dispersion on the carbon support after the EOR. Line scans and elemental composition (Figure 7(c-h)) indicate that Sn is partially leached from the nanocube shell, leading to the desired Pt-overlayer surface structure. No significant changes in the elemental distribution were observed by EDX analysis after reaction. Combining the STEM-EDX and HE-XRD findings suggests that the Sn is mainly accumulated in X-ray amorphous domains, which are stable under EOR conditions.

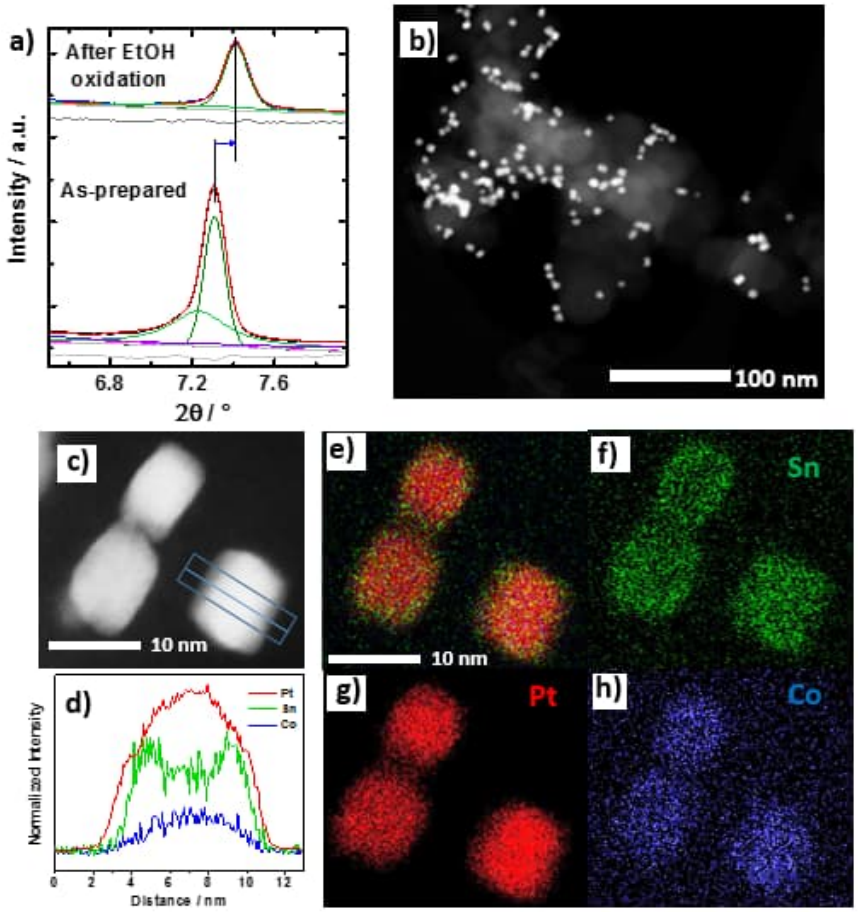


**Figure 7.** (a) Comparison of the XRD patterns for the Pt-Sn-Co catalyst before and after reaction. The fitted profiles were extracted by using Rietveld refinement. The experimental data of Pt, Pt-Sn, and Pt-Sn-Co are shown in black, red and blue, respectively. The fitted profiles are shown in red or black. The individual contributions from the fcc phase 1 (dark green), fcc phase 2 (light green), hcp phase (magenta), and from the carbon support (violet) are also shown as well as the corresponding background (dark grey) and difference curves (light grey). (b) ADF-STEM images of the Pt-Sn-Co NPs supported on Vulcan XC-72R after reaction. (c) EDX line-profiles recorded across the regions indicated by the arrow in (d). (e-h) EDX composition maps, showing Sn (green, f), Pt (red, g) and Co (blue, h) distributions.

In addition to the bulk structural and compositional properties, the surface composition and the presence of the surface metal oxide species in Pt-based electrocatalysts, especially $SnO_2$, has been discussed to affect the catalyst's EOR activity [46]. Thus, *quasi-in situ* XPS was used to investigate the Pt-Sn-Co nanocubes before and after reaction at 0.50 V for 1 h preceded by

the electrochemical activation process. Here, an electrochemical cell was directly attached to the UHV system, allowing a sample transfer without sample exposure to air. Figure 8 shows XPS spectra of the Pt-4f (a,c) and Sn-3d (b,d) core levels of the as-prepared state (a,b) and after EOR(c,d). The same spectra of the as-prepared Pt and Pt-Sn catalysts have also been included in Figure S4.

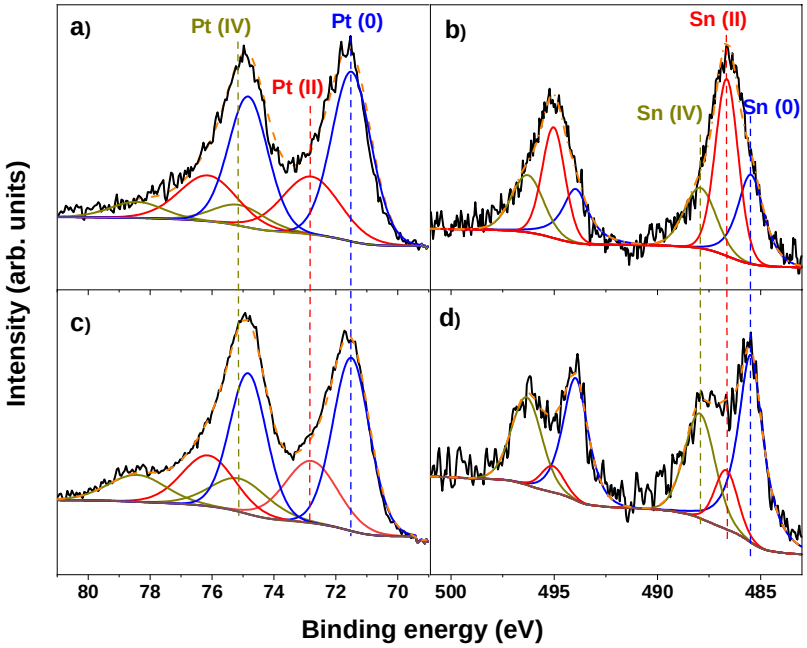


**Figure 8.** *Quasi in situ* XPS data of the (a,c) Pt-4f and (b,d) Sn-3d core level regions of Pt–Sn-Co nanocubes together with the corresponding fits acquired on the (a,b) as-prepared samples and (c,d) those after a 100 cycle activation pre-treatment and 1 h chronoamperometry at 0.5 V in 0.5 M $H_2SO_4$ + 1 M EtOH.

Co was not detected in the near-surface of the Pt-Sn-Co nanocubes before or after EOR, which is in agreement with the STEM-EDX findings as the Co 2p photoelectrons exhibit a kinetic energy close to 700 eV, leading to an inelastic mean free path as low as 1 nm in a Pt-rich material[47]. Table 2 and Table S2 summarize the surface composition as extracted from

the XPS spectra of the Pt-Sn-Co nanocubes and the as-prepared Pt and Pt-Sn catalysts, respectively.

| | at.% as-prepared | | | | | |
|---|---|---|---|---|---|---|
| Pt:Sn atomic ratio | Sn(0) | Sn(II) | Sn(IV) | Pt(0) | Pt(II) | Pt(IV) |
| 68:32 | 33 | 40 | 27 | 60 | 30 | 10 |
| | at.% after reaction | | | | | |
| Pt:Sn atomic ratio | Sn(0) | Sn(II) | Sn (IV) | Pt(0) | Pt(II) | Pt(IV) |
| 76:24 | 48 | 21 | 31 | 55 | 28 | 17 |

**Table 2.** Atomic percentages of the different Pt and Sn species on the surface of Pt-Sn-Co nanocubes extracted from the analysis of *quasi in situ* XPS data acquired before and after a 1 h chronoamperometry at 0.5 V in an Ar-purged 0.5 M $H_2SO_4$ + 1 M EtOH solution. No Co was detected on the surface (1 nm probing depth) of neither the as-prepared nor the samples after reaction.

The Pt:Sn atomic ratios before and after reaction were also determined from the analysis of the XPS data (Table 2). The surface composition analysis shows similar atomic percentages for the different Pt and Sn species present in the as-prepared Pt-Sn and Pt-Sn-Co NCs. Pt is partially metallic in both catalysts (60 at.% Pt(0) for Pt-Sn-Co and 65 at.% Pt(0) for Pt-Sn), whereas a higher content of metallic Pt (85 at.%) was found in the Pt catalyst. On the contrary, Sn was found to be mostly oxidize in both catalysts (40 at.% Sn(II) and 27 at.% of Sn(IV) for Pt-Sn-Co and (47 at.% Sn(II) and 23 at.% of Sn(IV) for Pt-Sn). In addition to providing information

on the surface composition, the Pt 4f spectra also indirectly reflect alterations in the position of the d-band center of the Pt atoms within the overlayer in the Pt-Sn-Co NCs. Peak fitting revealed a shift of 0.32 eV of the Pt 4f core-level to higher binding energies in the Pt-Sn-Co NCs before and after EOR as compared to the Pt-Sn NCs and Pt NCs (Figure S4d). In the case of $Pt_xCo$ and $Pt_xSn$ alloys, BE shifts in the range of +0.67 eV and -0.40eV have been reported, respectively [48,49]. Thus, the shift of the Pt 4f core level suggests a downward shift of the Pt d-band center of the Pt-Sn-Co NCs away from the Fermi level, revealing the influence of strain and/or ligand effects[50]. In the case of the Pt-Sn NCs, no shift in the Pt 4f core-level with respect to the Pt NCs could be observed.

An examination of the XPS spectra of the Pt-Sn-Co catalyst after reaction (Figure 8c and 8d and Table 2) show only a slight decrease in the fraction of Pt(0) (55 at.%) as well as a decrease in Sn(II) (21 at.% Sn(II) and 31 at.% of Sn(IV)) after the chronoamperometry. This decrease might be attributed to the dissolution of Sn(II) from the shell since it is unlikely that Sn(II) can be reduced to Sn(0) during the reaction at these anodic potentials. This indicates that the Sn contribution to the shell of the Pt−Sn-Co NCs before reaction, is primarily composed of Sn oxide species that become partially dissolve during the reaction.

An increase in the Pt:Sn atomic ratio was obtained (68:32 before reaction and 76:24 after reaction). This observation is in agreement with the partial leaching of Sn from the shell described above based on the chronoamperometry features and the TEM-EDX analysis, leading to the formation of Pt surface overlayer.

*In situ* X-ray absorption spectroscopy (XAS) providing element-specific information on the local structure of the bulk was used to probe significantly disordered phases. This is advantageous in the case of heterogeneous samples such as core-shell nanoparticles, where the

XRD pattern will almost exclusively show the contribution of well-ordered, crystalline (nanoparticle) phases. In contrast to XRD, XAS could be employed to monitor the changes in the sample structure *in situ* under electrocatalytic working conditions.

*In situ* X-ray absorption near edge structure (XANES) and Fourier-Transformed (FT-) EXAFS spectra for Pt $L_3$, Sn and Co K-edges for Pt-Sn-Co catalysts are shown in Figure 9. The corresponding spectra for the Pt-Sn and Pt NC samples are shown in Figure S5. For all samples, the Pt $L_3$-edge XANES and EXAFS spectra agree well with that of a Pt foil, suggesting that Pt is metallic and in a Pt-rich environment. The presence of a W $L_2$-edge feature below the Pt $L_3$-absorption edge shows the presence of residues from the $W(CO)_6$ used as a reducing agent for all three catalysts. EXAFS data fitting (Figure S6 and Table S3) confirms that in all samples the contribution of the Pt—Pt bonds is dominant. The presence of a significant and quantifiable number of Pt—Sn/Co bonds was not detected. However, slightly reduced coordination numbers in the Pt-Sn and Pt-Sn-Co NCs (with respect to the bulk fcc value of 12 and the Pt—Pt coordination number in pure Pt nanocubes) imply that some minor additional contribution (e.g., from Pt-Sn/Co) is present in the spectra. One can also note that the Pt-Pt distance is slightly shorter in the trimetallic sample as compared to the bimetallic one, in agreement with the XRD data.

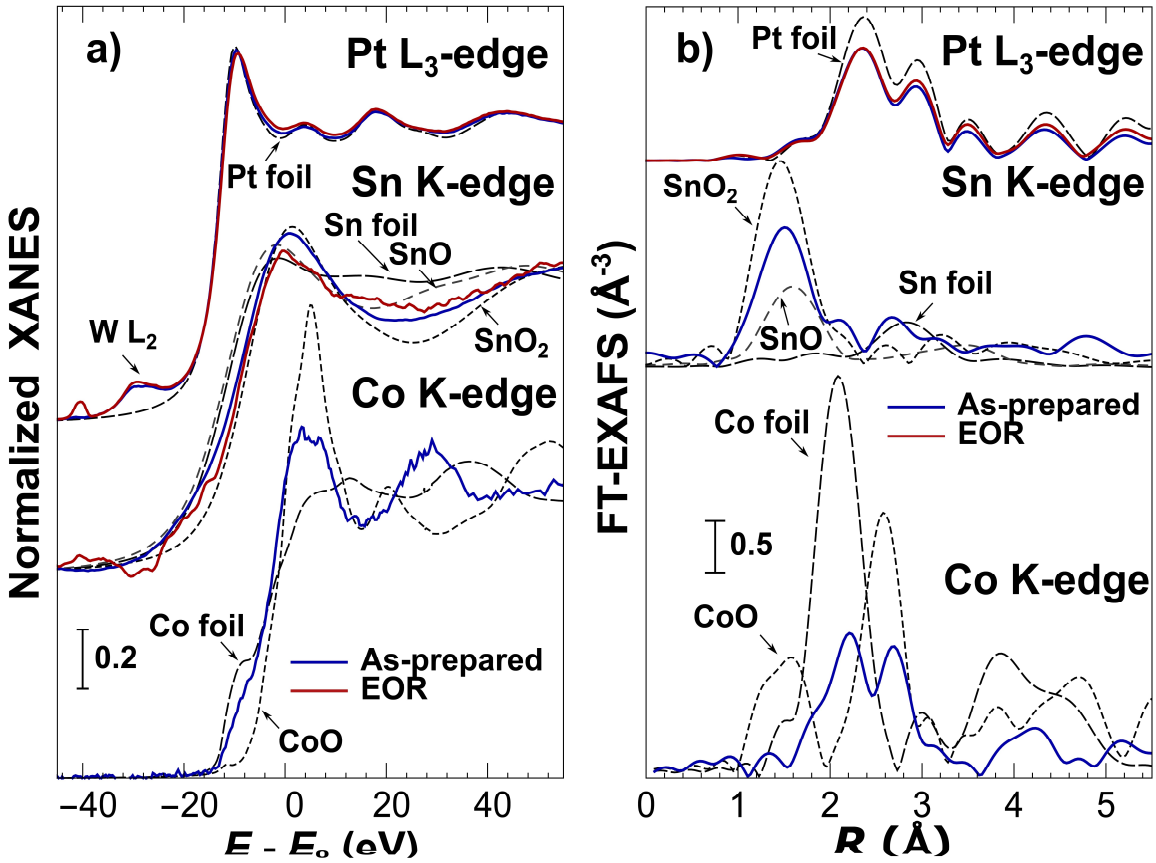


**Figure 9.** (a) *In situ* XANES and (b) and Fourier-transformed (FT) EXAFS data of Pt–Sn-Co nanocubes in as-prepared state (Pt-$L_3$, Sn K- and Co K-edges) and under reaction conditions (Pt-$L_3$ and Sn K edges) at 0.5 V during 1h in 0.5 M $H_2SO_4$ + 1 M ethanol.

The Co K-edge XANES and FT-EXAFS in the Pt-Sn-Co NCs are substantially different from those of the Co reference materials (both metallic Co and Co oxides) (Figure 9). The lack of features at low *R*-values in the Fourier-transformed Co K-edge EXAFS spectrum suggests that Co is in a metallic state and in a Pt-rich environment as the shape, position and intensity of the main features resemble those in the FT-EXAFS of Pt. A single Co-Pt contribution is sufficient to fit the EXAFS data yielding in a Co-Pt coordination number close to the bulk value of 12 (Figure S6 and Table S3). The Co—Pt interatomic distance (2.49 Å) is slightly shorter than the Pt—Pt bond length in metallic Pt (2.77 Å), in agreement with the smaller size of the

Co atom. These findings are in agreement with the XRD results, and XAS provides the key evidence that Co atoms are forming an alloy with Pt within the Pt-rich core of the Pt-Sn-Co NCs, and do not interact with Sn species.

XANES and FT-EXAFS for the Sn K-edge (Figure 9 and S6) show that Sn is (at least partially) oxidized in all samples. As no Sn oxide phases were detected by XRD, the Sn oxide domains are not crystalline. The position and shape of the main features in the Sn K-edge XANES and EXAFS spectra agree with those of the $SnO_2$ reference material. Nevertheless, the lower amplitude of the XANES features and of the main peak in the FT-EXAFS suggest that some fraction of Sn species is in a lower oxidation state. Linear combination analysis of the XANES data (Figure S7 and Table S4) shows that ca 55% of the Sn species in the as-prepared Pt-Sn-Co NCs, and 77% of the Sn species in the as-prepared Pt-Sn NC sample are in the 4+ state. Unfortunately, the low contrast between the SnO and Sn reference spectra does not allow a reliable quantification of Sn(II) and Sn(0) species. However, by comparing the results extracted from the analysis of the XANES, XRD and XPS data (Table 2), the presence of Sn(0) is inferred. The large fraction of Sn(IV) species is independently confirmed also by EXAFS data fitting (Figure S6 and Table S3), yielding a Sn-O bond length of 2.07 – 2.09 Å, which is close to that in $SnO_2$, and noticeably shorter than the Sn-O bond length in SnO (2.22 Å). The differences in the concentrations of different Sn species obtained by XAS and XPS is a result of the different sample depths probed by these techniques.

Under reaction conditions, analysis of the Pt $L_3$-edge spectra confirms the presence of a large Pt-rich core in all samples. In the case of the Pt-Sn nanocubes, a slight increase in the amplitude of the EXAFS features and in the Pt-Pt coordination number is agreement with a lower fraction of Pt-Sn distances and thus, with a leaching of Sn species from the Sn-containing

PtM alloy phases. Overall, the local atomic structure of the Pt was not significantly altered under reaction conditions.

*In situ* XAS at the Sn K-edge also revealed that the fraction of Sn(IV) does not significantly change in the Pt-Sn-Co NCs under reaction conditions, while it decreased by ca. 10% for the Pt-Sn NC sample. As explained above, the decrease in the concentration of oxidized Sn is likely a result of selective leaching of cationic Sn species from the nanocube shell. The leaching of Sn can be clearly seen in the XAS data. Figure S8 shows Sn K-edge spectra for catalysts in the as-prepared state and under reaction conditions. The spectra, collected in transmission mode, are background subtracted, but not normalized, thus capturing the difference in the number of absorbing Sn atoms showing a significant loss of Sn (20-30%). Larger leaching of Sn species for the Pt-Sn sample was detected as compared to the Pt-Sn-Co sample, in agreement with the more pronounced decrease in the concentration of Sn(IV) species observed for this sample from the linear combination analysis of the normalized XANES spectra.

Combining the findings from the electrochemical and physicochemical characterization as well as the insight from *in situ* and *operando* investigations, we found that the electrochemical activation and ethanol electroxidation reaction change the Pt-Sn-Co NCs as follows. Initially, the Pt-Sn-Co NCs consist of a Pt-Sn-Co core, with segregated partially oxidized Sn and metallic Co forming a $Pt_3Co$ alloy with Pt, which is decorated with a segregated partially oxidized Pt-Sn shell. The electrochemical activation induces significant Sn leaching and thus, generates electrochemically-accessible Pt(100) surface sites with low defect density, as identified by their voltammetric profiles. Those Pt surface sites can still interact with cationic Sn species available in the NC shell either as $Sn^{\delta+}$ adatoms, as an oxidized PtSn alloy as well as in the form of amorphous Sn oxide clusters (not detectable by XRD). The fraction of metallic PtSn significantly decreased after EOR as shown by HE-XRD, but a catalytic role of metallic Sn

cannot be excluded as the near-surface still contains Sn. Additionally, the core in the Pt-Sn-Co NCs shows a contracted lattice typical of a $Pt_3Co$ alloy, in contrast to the Pt-like core after EOR in the Pt-Sn NCs. The presence of Co in the Pt overlayer could not be experimentally confirmed.

Finally, our study demonstrates that the synergistic combination of Sn, Co and Pt results in an improved electro-oxidation of ethanol to carbon dioxide. Furthermore, it is highlight that the as-synthesized catalyst is very different from the active catalyst, and that *in situ* and *operando* characterization measurements are key in order to extract mechanistic understanding of electrocatalytic processes in complex nanostructured materials.

## 3. Conclusions

The synthesis and characterization of shape-controlled cubic Pt-Sn-Co electrocatalysts for ethanol oxidation reaction (EOR) is reported here. *Ex situ* TEM-EDX and XRD, *quasi in situ* XPS analysis, as well as *operando* XAS revealed the core-shell structures in the as-prepared state, with a Pt-Sn shell and Pt-Sn-Co core. After electrochemical activation and during EOR the nanocube morphology is preserved, while Sn partially leaches from the nanocubes, resulting in electrochemically accessible Pt surface sites on a Sn-poor $Pt_3Co$ core. This particular metal combination and morphological distribution was found to lead to a superior electrocatalytic activity as compared to similar Pt-Sn and Pt nanocubes. *In situ* DEMS showed the formation of volatile reaction intermediates and products such as acetaldehyde/acetic acid and an increased $CO_2$ conversion efficiency by the addition of Co to the Pt-Sn electrocatalyst. A key property here is the increased CO tolerance which explains the excellent performance of this trimetallic formulation towards the EOR.

## 4. Materials and methods

### 4.1 Reagents.

Tin(II) chloride dihydrate ($SnCl_2 \cdot 2H_2O$, 95%), platinum(II) acetylacetonate ($Pt(acac)_2$, 97%), cobalt(II) chloride hexahydrate ($CoCl_2 \cdot 6H_2O$, ≥97%), oleic acid (OA, 90%), oleylamine (OAm, 70%), tungsten hexacarbonyl ($W(CO)_6$, 99.99%) and acetic acid (HOAc, 96%) were acquired from Sigma-Aldrich. Ethanol (Reag. Ph. Eur) and n-hexane (96%) were purchased from Fisher Scientific Co.

### 4.2 Synthesis

Pt-Sn-Co nanocubes were synthesized by a solvothermal method using an OA/OAm mix as crystallization control agents[51]. First, $Pt(acac)_2$ (0.025 mmol) and $CoCl_2 \cdot 6H_2O$ (0.025 mmol) were mixed into a three-neck flask equipped with a condenser containing 8 mL of OA and 2 mL of OAm. Then, the temperature of the solution was increased to 130°C under stirring in inert atmosphere (Argon). Once this temperature was reached, 0.108 mmol of the reducing agent $W(CO)_6$ were added inside the flask containing the metal precursors while turning off the flow of Argon. Subsequently, 0.025 mmol of $SnCl_2 \cdot 2H_2O$ dissolved in 4 mL OLA and 1 mL OA were slowly added into the flask and the temperature was increased to 230°C. After 30 min at this temperature, the solution was cooled down to room temperature and the resulting NPs were washed several times with a hexane/ethanol (2:1) solution. The NPs were finally dispersed in hexane and impregnated in carbon (Vulcan XC-72R) by mixing the solution with the NPs with the appropriate amount of carbon dissolved in n-hexane in ultrasonication conditions overnight, to obtain a total metal loading of 20 wt %. The Pt-Sn-Co/C electrocatalyst was dispersed in acetic acid and the dispersion was heated at 60 °C under stirring conditions during

6 h. Finally, the supported electrocatalyst was washed with ethanol, filtered, washed again with Milli-Q water (Millipore), and dried at 60°C in an oven.

### 4.3 Physico-chemical characterization

The Pt-Sn-Co nanocubes supported on Vulcan XC-72R were characterized by X-ray diffraction (XRD) on a Bruker D8 Advance diffractometer with Cu $K_\alpha$ radiation ($\lambda$=1.5406 Å). High energy XRD measurements were also performed at ID31 of the European Synchrotron Radiation Facility (ESRF). The photon energy was set to 70 keV and the working distance was calibrated using a $CeO_2$ standard. Rietveld refinement was performed to analyze the laboratory and synchrotron diffraction patterns taking into account instrumental broadening, zero error and sample displacement. *Quasi in situ* X-ray photoelectron spectroscopy (XPS) experiments were performed in an electrochemical cell directly attached to the XPS-UHV system, allowing sample transfer without air exposure[52]. The XPS spectra were acquired using a non-monochromatic Al $K_\alpha$ source ($h\nu$ = 1486.5 eV) and a hemispherical Phoibos 100 analyzer (SPECS GmbH). The Pt spectra were deconvoluted with three doublets corresponding to Pt(0), Pt(II), and Pt(IV) species at 71.5 (Pt $4f_{7/2}$), 72.8, and 75.1 eV, respectively. The Sn spectra were deconvoluted with three doublets assigned to Sn(0) at 485.5 eV (Sn-3d3/2), Sn(II) at 486.6 eV and Sn (IV) at 488.0 eV. Annular dark-field (ADF) scanning transmission electron microscopy (STEM) measurements were performed with a JEOL microscope (JEM-2800) with a Schottky-type emission source at 200 kV and double SDD energy dispersive X-ray spectroscopy (EDX) detector.

*In-situ* X-ray absorption spectra at Pt $L_3$-edge (11.6 keV) data and Sn K-edge (29.2 keV) data were collected at PETRA-III synchrotron radiation facility at beamline P65 using a home-made electrochemical cell, where the sample was deposited on a carbon electrode and mounted

on a Kapton window. All samples were measured in air and under *operando* conditions (at 0.5 V in deoxygenated 0.5 M $H_2SO_4$ solution (Merck, 98%) with 1 M EtOH (Merck, p.a.)). For measurements at the Sn K-edge, a Si(311) double crystal monochromator was used for energy selection, and a Rh-coated collimating mirror for the removal of higher harmonics. For measurements at the Pt $L_3$-edge, Si(111) and a Si mirror were used instead. Measurements were performed in fluorescence mode using a PIPS detector. Transmission data were also collected for the Sn K-edge with samples in pellet form. Due to low sample loading, the transmission data are, overall, of lower quality than fluorescence data. However, they are useful for the estimation of the relative metal concentrations and their changes during the experiment, and were also used for the analysis in the case of Sn K-edge data in the Pt-Sn-Co material under reaction conditions, where the fluorescence signal was compromised by significant elastic scattering. *Ex situ* Co K-edge (7.7 keV) data were collected ad CLAESS beamline at ALBA synchrotron radiation facility. Due to the low Co concentration, *in-situ* data collection was not possible for the Co K-edge. Measurements were performed in fluorescence mode using an energy-selective 6 channel Si drifts detector. A Si(111) monochromator was used for energy selection. Alignment, background subtraction and normalization of XAS spectra were performed using the Athena software[53]. Extended X-ray absorption fine structure (EXAFS) spectra were fitted using the FEFFIT code. See supporting information for more details on EXAFS data fitting.

### 4.4 Electrochemical Characterization

All the EOR electrochemical measurements were performed in a deoxygenated 0.5 M $H_2SO_4$ aqueous solution (98%, Merck) with 1.0 M ethanol (Merck, p.a.). The electrochemical setup consisted of a Biologic potentiostat (SP-200) connected to a three-electrode configuration cell

with a reversible hydrogen electrode (RHE) reference and a high surface carbon rod as a counter electrode. An electrocatalyst ink was prepared by dispersing 2 mg of the electrocatalyst in a solution with 15 μL of Nafion (5 wt. %) and 500 μL ultrapure water (Millipore) in an ultrasound bath, and 20 μL of this ink was deposited onto a glassy carbon working electrode and dried under Ar atmosphere. Cyclic voltammograms (CVs) were recorded between 0.05 and 0.90 V vs RHE, and the electrochemically active surface area (ECSA) was calculated by the electrooxidation of an adsorbed CO monolayer on Pt using a surface area-specific charge of 420 μC $cm^{-2}$. [54] The CO stripping experiments were carried out by bubbling CO gas (99.997%, Air Liquide) for 10 min stepping the potential at 0.1 V, then removing non-adsorbed CO by bubbling Ar inside the electrochemical cell for 30 min, and subsequently scanning the cyclic voltammetry to a potential up to 0.9 V at 5 mV $s^{-1}$. Current transient curves were recorded at 0.50 V during 3600 s in the presence of ethanol.

For the differential electrochemical mass spectrometry (DEMS) experiments and the detection of gaseous and volatile products and intermediates during the reaction, a Hiden HPR-20 mass spectrometer connected to the electrochemical cell with a similar configuration to the one in Ref. [36] was used. The working electrode consists of a glassy carbon disk of a diameter of 7 mm with a hole in the center connected to the inlet of the mass spectrometer through a Teflon tube with inner diameter of 1/16 inches. A small piece of a Teflon membrane (Cobetter ®) was placed in the hole and 10 μL of the catalytic ink were deposited and dried on the membrane. In this way, mass spectrometry cyclic voltammograms (MSCVs) could be recorded in a meniscus configuration simultaneously with the corresponding cyclic voltammograms (CVs) recorded with an Autolab potentiostat (PGSTAT 302N). The efficiency of the conversion of ethanol to $CO_2$ was calculated by using the following equation:

$$E_{CO_2} = \frac{6*Q_i^{co_2}}{Q_f^T * K^{CO_2}}$$

where $Q_f^T$ and $Q_i^{co_2}$ correspond to the faradaic and ionic $m/z = 22$ charges, respectively, produced during the EOR. $K^{CO_2}$ is the calibration constant of the $m/z = 22$ calculated from the CO stripping experiments, which correlates the number of $CO_2$ molecules generated during the reaction and the amount of these molecules detected by the spectrometer[36]. Ohmic drops (solution resistance R ≈ 5 Ω) were compensated in recording all the CVs by using the IR-compensation mode of the potentiostat.

## Acknowledgments

This work was funded by the European Research Council under grant ERC-OPERANDOCAT (ERC-725915) and the Deutsche Forschungsgemeinschaft (DFG, German Research Foundation) under Germany's Excellence Strategy, EXC 2008/1 (UniSysCat), 390540038. Some of the TEM work was supported by the Cluster of Excellence RESOLV at RUB (EXC 1069) funded by the Deutsche Forschungsgemeinschaft (DFG).

## References


[1] D. Banham, S. Ye, Current status and future development of catalyst materials and catalyst layers for proton exchange membrane fuel cells: an industrial perspective, ACS Energy Lett. 2 (2017) 629–638.

[2] M.K. Debe, Electrocatalyst approaches and challenges for automotive fuel cells, Nature. 486 (2012) 43-51.

[3] Y. Choi, I. Sinev, H. Mistry, I. Zegkinoglou, B. Roldan Cuenya, Probing the Dynamic Structure and Chemical State of Au Nanocatalysts during the Electrochemical Oxidation of 2-Propanol, ACS Catal. 6 (2016) 3396–3403.

[4] R. Rizo, R.M. Arán-Ais, E. Padgett, D.A. Muller, M.J. Lázaro, J. Solla-Gullón, J.M. Feliu, E. Pastor, H.D. Abruña, Pt-Richcore/Sn-Richsubsurface/Ptskin Nanocubes As Highly Active and Stable Electrocatalysts for the Ethanol Oxidation Reaction, J. Am. Chem. Soc. 140 (2018) 3791–3797.

[5] Z. Zhang, Q. Wu, K. Mao, Y. Chen, L. Du, Y. Bu, O. Zhuo, L. Yang, X. Wang, Z. Hu, Efficient Ternary Synergism of Platinum/Tin Oxide/Nitrogen-doped Carbon Leading to High-Performance Ethanol Oxidation, ACS Catal. (2018) 8477-8483.

[6] E. Antolini, Catalysts for direct ethanol fuel cells, J. Power Sources. 170 (2007) 1–12.

[7] M.J.S. Farias, W. Cheuquepán, A.A. Tanaka, J.M. Feliu, Unraveling the Nature of Active Sites in Ethanol Electro-oxidation by Site-Specific Marking of a Pt Catalyst with Isotope-Labeled $^{13}CO$, J. Phys. Chem. Lett. 9 (2018) 1206–1210.

[8] T. Iwasita, E. Pastor, DEMS and FTIR spectroscopic investigation of adsorbed ethanol on polycrystalline platinum, Electrochim. Acta. 39 (1994) 531–537.

[9] L. Huang, X. Zhang, Q. Wang, Y. Han, Y. Fang, S. Dong, Shape-Control of Pt–Ru Nanocrystals: Tuning Surface Structure for Enhanced Electrocatalytic Methanol Oxidation, J. Am. Chem. Soc. 140 (2018) 1142–1147.

[10] F.H.B. Lima, E.R. Gonzalez, Ethanol electro-oxidation on carbon-supported Pt–Ru, Pt–Rh and Pt–Ru–Rh nanoparticles, Electrochim. Acta. 53 (2008) 2963–2971.

[11] B.-W. Zhang, T. Sheng, Y.-X. Wang, X.-M. Qu, J.-M. Zhang, Z.-C. Zhang, H.-G. Liao, F.-C. Zhu, S.-X. Dou, Y.-X. Jiang, Platinum–cobalt bimetallic nanoparticles with Pt skin for electro-oxidation of ethanol, ACS Catal. 7 (2016) 892–895.

[12] A. Kowal, M. Li, M. Shao, K. Sasaki, M.B. Vukmirovic, J. h Zhang, N.S. Marinkovic, P. Liu, A.I. Frenkel, R.R. Adzic, Ternary Pt/Rh/$SnO_2$ electrocatalysts for oxidizing ethanol to $CO_2$, Nat. Mater. 8 (2009) 325-330.

[13] R. Rizo, D. Sebastián, M.J. Lázaro, E. Pastor, On the design of Pt-Sn efficient catalyst for carbon monoxide and ethanol oxidation in acid and alkaline media, Appl. Catal. B Environ. 200 (2017) 246–254.

[14] R. Rizo, E. Pastor, M.T.M. Koper, CO electrooxidation on Sn-modified Pt single crystals in acid media, J. Electroanal. Chem. 800 (2017) 32–38.

[15] V.R. Stamenkovic, B.S. Mun, K.J.J. Mayrhofer, P.N. Ross, N.M. Markovic, Effect of surface composition on electronic structure, stability, and electrocatalytic properties of Pt-transition metal alloys: Pt-skin versus Pt-skeleton surfaces, J. Am. Chem. Soc. 128 (2006) 8813–8819.

[16] K. Wang, H. Du, R. Sriphathoorat, P.K. Shen, Vertex-Type Engineering of Pt–Cu–Rh Heterogeneous Nanocages for Highly Efficient Ethanol Electrooxidation, Adv. Mater. 30 (2018) 1804074.

[17] E.A. de Souza, M.J. Giz, G.A. Camara, E. Antolini, R.R. Passos, Ethanol electro-oxidation on partially alloyed Pt-Sn-Rh/C catalysts, Electrochim. Acta. 147 (2014) 483–489.

[18] N. Erini, S. Rudi, V. Beermann, P. Krause, R. Yang, Y. Huang, P. Strasser, Exceptional activity of a Pt–Rh–Ni ternary nanostructured catalyst for the electrochemical oxidation of ethanol, ChemElectroChem. 2 (2015) 903–908.

[19] A.B. Delpeuch, T. Asset, M. Chatenet, C. Cremers, Electrooxidation of ethanol at room temperature on carbon-supported Pt and Rh-containing catalysts: A DEMS study, J. Electrochem. Soc. 161 (2014) F918–F924.

[20] V. Del Colle, J. Souza-Garcia, G. Tremiliosi-Filho, E. Herrero, J.M. Feliu, Electrochemical and spectroscopic studies of ethanol oxidation on Pt stepped surfaces modified by tin adatoms., Phys. Chem. Chem. Phys. 13 (2011) 12163–72.

[21] R. Rizo, M.J. Lázaro, E. Pastor, M. Koper, Ethanol Oxidation on Sn-modified Pt Single-Crystal Electrodes: New Mechanistic Insights from Online Electrochemical Mass Spectrometry, ChemElectroChem. 3 (2016) 2196–2201.

[22] Y. Zheng, J. Qiao, J. Yuan, J. Shen, A. Wang, S. Huang, Controllable synthesis of PtPd

nanocubes on graphene as advanced catalysts for ethanol oxidation, Int. J. Hydrogen Energy. 43 (2018) 4902–4911.

[23] L. Rao, Y.-X. Jiang, B.-W. Zhang, Y.-R. Cai, S.-G. Sun, High activity of cubic PtRh alloys supported on graphene towards ethanol electrooxidation, Phys. Chem. Chem. Phys. 16 (2014) 13662–13671.

[24] Q. Chang, S. Kattel, X. Li, Z. Liang, B.M. Tackett, S.R. Denny, P. Zhang, D. Su, J.G. Chen, Z. Chen, Enhancing C–C Bond Scission for Efficient Ethanol Oxidation using PtIr Nanocube Electrocatalysts, ACS Catal. 9 (2019) 7618–7625.

[25] P. Li, K. Liu, J. Ye, F. Xue, Y. Cheng, Z. Lyu, X. Liao, W. Wang, Q. Zhang, X. Chen, Facilitating the C–C bond cleavage on sub-10 nm concavity-tunable Rh@ Pt core–shell nanocubes for efficient ethanol electrooxidation, J. Mater. Chem. A. 7 (2019) 17987–17994.

[26] W. Zhu, J. Ke, S.-B. Wang, J. Ren, H.-H. Wang, Z.-Y. Zhou, R. Si, Y.-W. Zhang, C.-H. Yan, Shaping single-crystalline trimetallic Pt–Pd–Rh nanocrystals toward high-efficiency C–C splitting of ethanol in conversion to $CO_2$, Acs Catal. 5 (2015) 1995–2008.

[27] Z. Liu, J. Qi, M. Liu, S. Zhang, Q. Fan, H. Liu, K. Liu, H. Zheng, Y. Yin, C. Gao, Aqueous Synthesis of Ultrathin Platinum/Non-Noble Metal Alloy Nanowires for Enhanced Hydrogen Evolution Activity, Angew. Chemie. 130 (2018) 11852–11856.

[28] P.E. Tsiakaras, PtM/C (M= Sn, Ru, Pd, W) based anode direct ethanol–PEMFCs: structural characteristics and cell performance, J. Power Sources. 171 (2007) 107–112.

[29] A.J. Wain, M.A. O'Connell, G.A. Attard, Insights into Self-Poisoning during Catalytic Hydrogenation on Platinum Surfaces Using ATR-IR Spectroelectrochemistry, ACS Catal. 8 (2018) 3561–3570.

[30] F.J. Vidal-Iglesias, J. Solla-Gullón, V. Montiel, J.M. Feliu, A. Aldaz, Screening of electrocatalysts for direct ammonia fuel cell: ammonia oxidation on PtMe (Me: Ir, Rh, Pd, Ru) and preferentially oriented Pt (1 0 0) nanoparticles, J. Power Sources. 171 (2007) 448–456.

[31] F.J. Vidal-Iglesias, R.M. Arán-Ais, J. Solla-Gullón, E. Herrero, J.M. Feliu, Electrochemical characterization of shape-controlled Pt nanoparticles in different supporting electrolytes, ACS Catal. 2 (2012) 901–910.

[32] S. Rudi, C. Cui, L. Gan, P. Strasser, Comparative study of the electrocatalytically active surface areas (ECSAs) of Pt alloy nanoparticles evaluated by H upd and CO-stripping voltammetry, Electrocatalysis. 5 (2014) 408–418.

[33] D.F. van der Vliet, C. Wang, D. Li, A.P. Paulikas, J. Greeley, R.B. Rankin, D. Strmcnik, D. Tripkovic, N.M. Markovic, V.R. Stamenkovic, Unique electrochemical adsorption properties of Pt-Skin Surfaces, Angew. Chemie Int. Ed. 51 (2012) 3139–3142.

[34] C. Wei, R.R. Rao, J. Peng, B. Huang, I.E.L. Stephens, M. Risch, Z.J. Xu, Y. Shao-Horn, Recommended practices and benchmark activity for hydrogen and oxygen electrocatalysis in water splitting and fuel cells, Adv. Mater. 31 (2019) 1806296.

[35] N. Shakibi Nia, O. Guillén-Villafuerte, C. Griesser, G. Manning, J. Kunze-Liebhäuser, C. Árevalo, E. Pastor, G. Garcia, $W_2C$-supported PtAuSn–a catalyst with the earliest ethanol oxidation onset potential and the highest ethanol conversion efficiency to $CO_2$ known to date, ACS Catal. (2019) 1113-1122.

[36] R. Rizo, D. Sebastián, J.L. Rodríguez, M.J. Lázaro, E. Pastor, Influence of the nature of the carbon support on the activity of Pt/C catalysts for ethanol and carbon monoxide oxidation, J. Catal. 348 (2017) 22–28.

[37] A. Winiwarter, L. Silvioli, S.B. Scott, K. Enemark-Rasmussen, M. Sariç, D.B. Trimarco, P.C.K. Vesborg, P.G. Moses, I.E.L. Stephens, B. Seger, Towards an atomistic understanding of electrocatalytic partial hydrocarbon oxidation: propene on palladium, Energy Environ. Sci. 12 (2019) 1055–1067.

[38] J. Rossmeisl, P. Ferrin, G.A. Tritsaris, A.U. Nilekar, S. Koh, S.E. Bae, S.R. Brankovic, P. Strasser, M. Mavrikakis, Bifunctional anode catalysts for direct methanol fuel cells, Energy Environ. Sci. 5 (2012) 8335–8342.

[39] A. De Clercq, O. Margeat, G. Sitja, C.R. Henry, S. Giorgio, Core–shell Pd–Pt nanocubes for the CO oxidation, J. Catal. 336 (2016) 33–40.

[40] F.C.H. Lim, J. Zhang, H. Jin, M.B. Sullivan, P. Wu, A density functional theory study of CO oxidation on Pd-Ni alloy with sandwich structure, Appl. Catal. A Gen. 451 (2013) 79–85.

[41] T. Bligaard, J.K. Nørskov, Ligand effects in heterogeneous catalysis and electrochemistry, Electrochim. Acta. 52 (2007) 5512–5516.

[42] V. Stamenkovic, B.S. Mun, K.J.J. Mayrhofer, P.N. Ross, N.M. Markovic, J. Rossmeisl, J. Greeley, J.K. Nørskov, Changing the activity of electrocatalysts for oxygen reduction by tuning the surface electronic structure, Angew. Chemie Int. Ed. 45 (2006) 2897–2901.

[43] N.S. Nia, A. Martucci, G. Granozzi, G. García, E. Pastor, S. Penner, J. Bernardi, N. Alonso-Vante, J. Kunze-Liebhäuser, DEMS studies of the ethanol electro-oxidation on TiOC supported Pt catalysts–Support effects for higher $CO_2$ efficiency, Electrochim. Acta. 304 (2019) 80–86.

[44] D.A. Cantane, W.F. Ambrosio, M. Chatenet, F.H.B. de Lima, Electro-oxidation of ethanol on Pt/C, Rh/C, and Pt/Rh/C-based electrocatalysts investigated by on-line DEMS, J. Electroanal. Chem. 681 (2012) 56–65.

[45] L. Colmenares, H. Wang, Z. Jusys, L. Jiang, S. Yan, G.Q. Sun, R.J. Behm, Ethanol oxidation on novel, carbon supported Pt alloy catalysts—model studies under defined diffusion conditions, Electrochim. Acta. 52 (2006) 221–233.

[46] H. Wang, Z. Liu, S. Ji, K. Wang, T. Zhou, R. Wang, Ethanol oxidation activity and structure of carbon-supported Pt-modified PdSn-$SnO_2$ influenced by different stabilizers, Electrochim. Acta. 108 (2013) 833–840.

[47] C.J. Powell, A. Jablonski, NIST electron inelastic-mean-free-path database, NIST Stand. Ref. Database. 71 (2010).

[48] M.E. Scofield, Y. Zhou, S. Yue, L. Wang, D. Su, X. Tong, M.B. Vukmirovic, R.R. Adzic, S.S. Wong, Role of chemical composition in the enhanced catalytic activity of Pt-based alloyed ultrathin nanowires for the hydrogen oxidation reaction under alkaline conditions, ACS Catal. 6 (2016) 3895–3908.

[49] G. Samjeské, S. Nagamatsu, S. Takao, K. Nagasawa, Y. Imaizumi, O. Sekizawa, T. Yamamoto, Y. Uemura, T. Uruga, Y. Iwasawa, Performance and characterization of a Pt–Sn (oxidized)/C cathode catalyst with a $SnO_2$-decorated $Pt_3Sn$ nanostructure for oxygen reduction reaction in a polymer electrolyte fuel cell, Phys. Chem. Chem. Phys. 15 (2013) 17208–17218.

[50] H. Mistry, A.S. Varela, S. Kühl, P. Strasser, B.R. Cuenya, Nanostructured electrocatalysts with tunable activity and selectivity, Nat. Rev. Mater. 1 (2016) 1–14.

[51] J. Zhang, J. Fang, A general strategy for preparation of Pt 3d-transition metal (Co, Fe,

Ni) nanocubes, J. Am. Chem. Soc. 131 (2009) 18543–18547.

[52] M. Bernal, A. Bagger, F. Scholten, I. Sinev, A. Bergmann, M. Ahmadi, J. Rossmeisl, B.R. Cuenya, $CO_2$ Electroreduction on Copper-Cobalt Nanoparticles: Size and Composition Effect, Nano Energy. (2018) 27-36.

[53] B. Ravel, M. Newville, ATHENA, ARTEMIS, HEPHAESTUS: data analysis for X-ray absorption spectroscopy using IFEFFIT, J. Synchrotron Radiat. 12 (2005) 537–541.

[54] R.M. Arán-Ais, Y. Yu, R. Hovden, J. Solla-Gullón, E. Herrero, J.M. Feliu, H.D. Abruña, Identical location transmission electron microscopy imaging of site-selective Pt nanocatalysts: electrochemical activation and surface disordering, J. Am. Chem. Soc. 137 (2015) 14992–14998.